



**HAL**  
open science

# Fast Computation of Multi-Parametric Electromagnetic Fields in Synchronous Machines by Using PGD-Based Fully Separated Representations

Abel Sancarlos, Chady Ghnatios, Jean-Louis Duval, Nicolas Zerbib, Elias Cueto, Francisco Chinesta

## ► To cite this version:

Abel Sancarlos, Chady Ghnatios, Jean-Louis Duval, Nicolas Zerbib, Elias Cueto, et al.. Fast Computation of Multi-Parametric Electromagnetic Fields in Synchronous Machines by Using PGD-Based Fully Separated Representations. *Energies*, 2021, 14 (5), pp.1454. 10.3390/en14051454 . hal-03262622

**HAL Id: hal-03262622**




**<https://hal.science/hal-03262622>**

Submitted on 16 Jun 2021

**HAL** is a multi-disciplinary open access archive for the deposit and dissemination of scientific research documents, whether they are published or not. The documents may come from teaching and research institutions in France or abroad, or from public or private research centers.

L'archive ouverte pluridisciplinaire **HAL**, est destinée au dépôt et à la diffusion de documents scientifiques de niveau recherche, publiés ou non, émanant des établissements d'enseignement et de recherche français ou étrangers, des laboratoires publics ou privés.

# Fast Computation of Multi-Parametric Electromagnetic Fields in Synchronous Machines by Using PGD-Based Fully Separated Representations

Abel Sancarlos <sup>1,2,3</sup> , Chady Ghnatios <sup>4</sup> , Jean-Louis Duval <sup>2</sup>, Nicolas Zerbib <sup>2</sup>, Elias Cueto <sup>3</sup>  and Francisco Chinesta <sup>1,2,\*</sup>

<sup>1</sup> PIMM Lab and ESI Group Chair, Arts et Metiers Institute of Technology, 155 Boulevard de Hopital, F-75013 Paris, France; abel.sancarlos\_gonzalez@ensam.eu

<sup>2</sup> ESI Group, 3bis rue Saarinen, 94528 Rungis, France; Jean-Louis.Duval@esi-group.com (J.-L.D.); Nicolas.Zerbib@esi-group.com (N.Z.)

<sup>3</sup> Aragon Institute of Engineering Research, Universidad de Zaragoza, Maria de Luna, s.n., E-50018 Zaragoza, Spain; ecueto@unizar.es

<sup>4</sup> Mechanical Engineering Department, Notre Dame University-Louaize (NDU), Zouk Mosbeh 72, Lebanon; cghnatios@ndu.edu.lb

\* Correspondence: Francisco.Chinesta@ensam.eu

**Abstract:** A novel Model Order Reduction (MOR) technique is developed to compute high-dimensional parametric solutions for electromagnetic fields in synchronous machines. Specifically, the intrusive version of the Proper Generalized Decomposition (PGD) is employed to simulate a Permanent-Magnet Synchronous Motor (PMSM). The result is a virtual chart allowing real-time evaluation of the magnetic vector potential as a function of the operation point of the motor, or even as a function of constructive parameters, such as the remanent flux in permanent magnets. Currently, these solutions are highly demanded by the industry, especially with the recent developments in the Electric Vehicle (EV). In this framework, standard discretization techniques require highly time-consuming simulations when analyzing, for instance, the noise and vibration in electric motors. The proposed approach is able to construct a virtual chart within a few minutes of off-line simulation, thanks to the use of a fully separated representation in which the solution is written from a series of functions of the space and parameters coordinates, with full space separation made possible by the use of an adapted geometrical mapping. Finally, excellent performances are reported when comparing the reduced-order model with the more standard and computationally costly Finite Element solutions.

**Keywords:** Proper Generalized Decomposition (PGD); Model Order Reduction (ROM); reduced-order model; electric machine; electric motor; Permanent-Magnet Synchronous Motor (PMSM); real-time simulation; virtual chart

## 1. Introduction

Numerical tools such as the Finite Element Method (FEM) or the Finite Difference Method are powerful and excellent methodologies for analyzing static and dynamical systems. Despite this, a great portion of numerical simulations concerning real-life problems face difficulties in design, optimization and control due to the complexity of the system, high computational costs, and storage requirement [1,2].

At present, industry is permanently looking for fast and accurate solutions in electric motors and generators, and trends such as the Electric Vehicle or the self-driving car are producing a lot of investment in that direction. The reason for this seems clear: achieving these goals will improve the final design's performance and economic competitiveness.

To address this need, a model order reduction technique that employs the Proper Generalized Decomposition (PGD) is developed. This method alleviates the curse of



dimensionality through solving a Partial Differential Equation (PDE) or a set of PDEs in a high-dimensional space within minutes, using a separated representation of the multiparametric solution. Moreover, this technique has solved unfeasible high-dimensional problems with high accuracy, and its abilities have been proven in many previous works. The reader unfamiliar with the Proper Generalized Decomposition (PGD) method for solving PDEs can refer to [3,4] and the numerous references therein, where these parametric solutions were employed for predicting, optimizing, propagating uncertainty, performing inverse analysis and simulation-based control, all under the stringent real-time constraint. For the sake of completeness, the PGD procedure for constructing spatial and parametric separated representations is revisited in the Appendix A.

Such parametric solutions could be also applied in new technological applications, such as the modeling and control of imperfect dynamical systems [5] for monitoring, control and predictive and/or operational maintenance purposes. For that purpose, an appealing route consists of calculating the stochastic counterpart of these solutions with the parameters of mean value and the standard deviation.

PGD was previously applied in electromagnetics, such as, for instance, the computation of impedance in industrial busbar systems [6], the analysis of magnetoelectric devices [7] or batteries [8]. However, the complex non-separable geometry of electric motors limited its use for efficiently expressing the solution by separating the space coordinates. Furthermore, there is also a numerical challenge when introducing the rotor movement as a parameter in the PGD framework. In this work, a framework to efficiently employ the PGD for a Permanent-Magnet Synchronous Motor (PMSM) is set up. To overcome the complex geometries limitation, an adapted mapping of the real geometry into a suitable separable domain is proposed. Such mappings were previously successfully employed to deal with apparently non-separable domains [9,10].

To evaluate the obtained PGD solutions, the finite element software FEMM is employed. The main aim of using FEMM is twofold. First, it aims to make the results more accessible to the community for checking, with FEMM being an open-source finite-element analysis software package. Second, it aims to have a good reference to rely on. Furthermore, we would like to emphasize the fact that the PGD is, at present, a mature technique in the area of computational mechanics, where its efficiency has been largely proven. The reader can refer to the review papers [11,12] and the numerous references therein. The application of PGD-based techniques in electromagnetism constitutes a very active research area at present.

The main contributions of the present paper are: (i) the introduction of a very efficient geometrical mapping, able to separable render the motor geometry, enabling the application of the PGD-based space-separated representation; (ii) the introduction of other parameters as model extra-parameters, enabling the construction of parametric solutions to be efficiently used in a variety of engineering applications. The attained computational efficiency is impressive, attaining, thanks to the separated representation constructor, resolutions equivalent to  $10^{23}$  FEM degrees of freedom, within few minutes, on a standard laptop, performances which are unattainable when using more usual multi-purpose discretization techniques.

The paper is organized as follows. In Section 2, the physical equations are presented to focus on a two-dimensional steady-state analysis of a PMSM. Next, in Section 3, the simulated motor is presented where the main parameters/features are introduced. Then, in Section 4, the formulation for the separated PGD representation in space is presented. Furthermore, in Section 5, the formulation to add the parameters as extra-coordinates in the PGD framework is shown. Finally, in Sections 6 and 7, the results and general conclusions of the present work are addressed.

## 2. Electromagnetic Equations

A two-dimensional steady-state analysis (magneto-static analysis) is employed to analyze the synchronous machine.

In three-phase motors, as in the other polyphase configurations of the synchronous machines, the stator-produced magnetomotive force (MMF) rotates at synchronous speed. Since the rotor is also rotating at synchronous speed in the steady state, an observer on the rotor experiences a constant field ( $\frac{\partial \mathbf{B}}{\partial t} = \mathbf{0}$ ), and, therefore, there are no eddy currents on the rotor.

On the other hand, an observer on the stator experiences a time-varying field with a characteristic frequency. Since the stator is laminated and the stator windings are stranded and transposed, the eddy currents are limited and can be neglected in the field computation.

Taking into consideration the above assumptions, let us start with Ampere's law

$$\nabla \times \mathbf{H} = \mathbf{J}, \quad (1)$$

where  $\nabla$  is the nabla operator,  $\mathbf{J}$  is the electric current density and  $\mathbf{H}$  is the magnetic H-field. In addition, the magnetic flux density ( $\mathbf{B}$ -field) is related to the magnetic field strength ( $\mathbf{H}$ -field) using

$$\mathbf{B} = \mu_0(\mu_r \mathbf{H} + \mathbf{M}), \quad (2)$$

where  $\mathbf{M}$  is the magnetization vector,  $\mu_r$  is the relative magnetic permeability and  $\mu_0$  is the magnetic permeability of free space. Noting that  $\nu = \frac{1}{\mu_0 \mu_r}$  and combining Equations (1) and (2), one obtains

$$\nabla \times (\nu \mathbf{B}) = \mathbf{J} + \nabla \times (\nu \mu_0 \mathbf{M}). \quad (3)$$

Using the Helmholtz decomposition and noting that  $\nabla \cdot \mathbf{B} = 0$ , the B-field can be expressed as

$$\mathbf{B} = \nabla \times \mathbf{A}, \quad (4)$$

with  $\mathbf{A}$  is the magnetic vector potential, leading to

$$\nabla \times (\nu \nabla \times \mathbf{A}) = \mathbf{J} + \nabla \times (\nu \mu_0 \mathbf{M}). \quad (5)$$

Note that eventhough the gauge condition should be defined for 3D, the condition is automatically satisfied for 2D problems. To define the integral form of the problem,  $\mathbf{W}$  is used as the test function

$$\int_{\Omega} \nabla \times (\nu \nabla \times \mathbf{A} - \nu \mu_0 \mathbf{M}) \cdot \mathbf{W} d\Omega = \int_{\Omega} \mathbf{J} \cdot \mathbf{W} d\Omega. \quad (6)$$

As detailed in [13], after using some vector identities and the divergence theorem, the results are

$$\int_{\Omega} \nu (\nabla \times \mathbf{A}) \cdot (\nabla \times \mathbf{W}) d\Omega = \int_{\Omega} \nu \mu_0 \mathbf{M} \cdot (\nabla \times \mathbf{W}) d\Omega + \int_{\Omega} \mathbf{W} \cdot \mathbf{J} d\Omega, \quad (7)$$

that in the 2D case reads

$$\int_{\Omega} \nu \left( \frac{\partial A_z}{\partial x} \frac{\partial W}{\partial x} + \frac{\partial A_z}{\partial y} \frac{\partial W}{\partial y} \right) d\Omega = \int_{\Omega} \left( \nu \mu_0 \left( M_x \frac{\partial W}{\partial y} - M_y \frac{\partial W}{\partial x} \right) + J_z W \right) d\Omega \quad (8)$$

### 3. Description of the Analyzed Motor

An example from the FEMM software manual [14] is borrowed, where geometry and further details can be found. The main parameters and features of the motor are as follows:

- Three-phase supply. This is an eight-pole machine (i.e.,  $p = 4$ );
- The winding configuration for one pole of the machine is: A+, B-, C+ (the three slots from 0 to 45 geometrical degrees).

The motor geometry is characterized by:

- Rotor Inner Diameter: 22.8 mm;
- Rotor Iron Outer Diameter: 50.5 mm;

- Rotor Outer Diameter: 55.1 mm;
- Air Gap Length: 0.7 mm;
- Stator Outer Diameter: 100 mm;
- Angle Spanned by Tooth: 11.9 deg;
- Turns/Slot: 46;
- The complete geometry of the machine is shown in Figure 1.

In turn, the considered materials are:

- Winding Wire: 4X20AWG copper wire;
- Magnet Material: Sm2Co17 24MGOe;
- Stator Material: 24 Gauge M19 NGO Steel @ 98% fill;
- Rotor Material: 1018 steel.

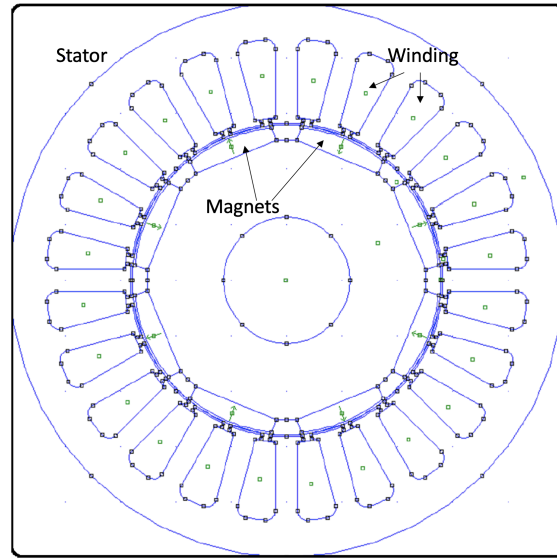


**Figure 1.** Electric machine to simulate. The green arrow in the permanent magnets indicates the magnetization direction.

#### 4. PGD Physical Space Separated Solution

The domain of simulation is not suitable for a PGD-separated representation using Cartesian  $(x, y)$  coordinates because of the lack of plane symmetries (see Figure 1). Previous techniques were developed to deal with such complexity using the PGD framework [15]. However, in this work, a new suitable mapping to transform the motor geometry into the one shown in Figures 2 and 3 is developed. The advantage is that the resultant geometry is amenable for a separated representation within the PGD framework.

The first step to achieving this goal is to perform a mapping to the polar coordinates  $(R, \theta)$  using

$$\begin{cases} R = \sqrt{x^2 + y^2} \\ \theta = \arctg\left(\frac{y}{x}\right) \end{cases} \quad (9)$$

where  $\arctg$  is the inverse trigonometric function arctangent.

Then, a second mapping is used to transform the resulting non-fully separable domain into a prismatic, easily separable one,  $(s, t)$ , such as  $s \in [1, 7]$  and  $t \in [0, 2\pi)$ , using the following transformation, for  $i = 2, \dots, 7$

$$\begin{cases} R(s \in [i-1, i], t) = [s - (i-1)] \cdot (h_i(t) - h_{i-1}(t)) + h_{i-1}(t) \\ \theta(s, t \in [0, 2\pi)) = t \end{cases}, \quad (10)$$

where  $s$  and  $t$  are the new coordinates and  $i$  is computed rounding up the  $s$  value to the next integer. In addition, the integers of the  $s$  coordinate are placed strategically, as shown in Figure 4, and the definition of  $h_i(t)$  functions is illustrated in Figure 5.

Using the associated Jacobians and the chain rule, one can rewrite the weak form (8) into the  $(s, t)$  domain. More details about this technique can be found in [9,10,16].

The domain depicted in Figure 3 can be easily expressible by using a fully space-separated representation within the PGD rationale, by expressing in the same way the material properties, e.g.,

$$v(s, t) = \sum_{k=1}^n S_k(s) \mathcal{T}_k(t) \quad (11)$$

where  $n$  is the number of needed products.

By replacing the mapping into Equation (8), one may find the final weak form of the problem by using the corresponding 1D-1D meshes defined in  $s$  and  $t$  one-dimensional domains. The separated representations of the other known functions  $J_z$  and  $\mathbf{M}$  is detailed in the next section.

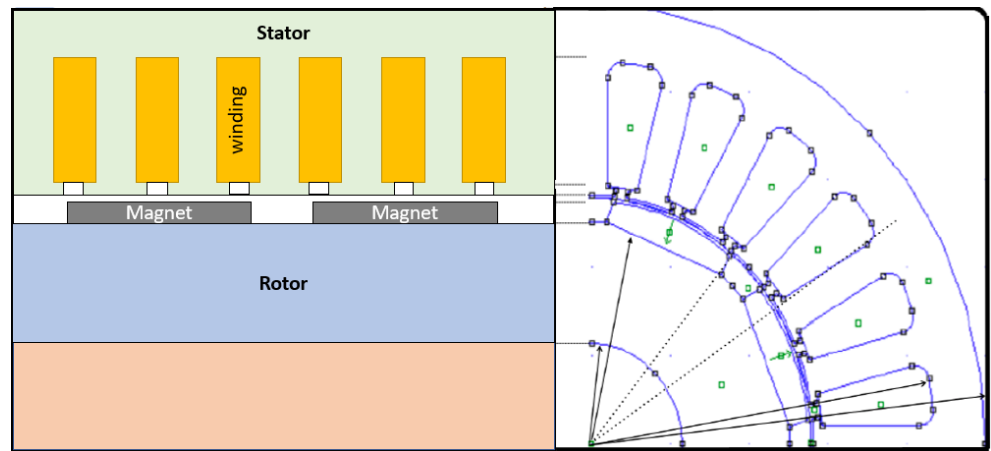


Figure 2. Mapping from the original geometry into the calculation one.

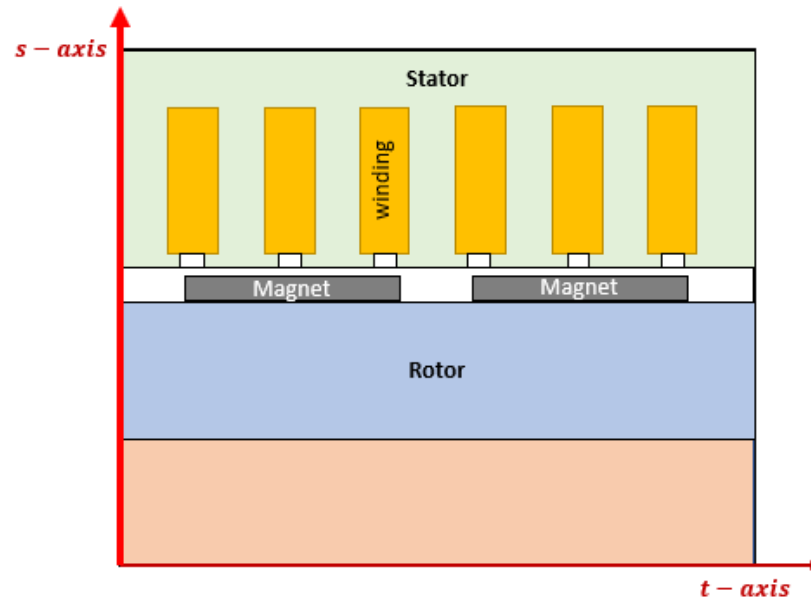
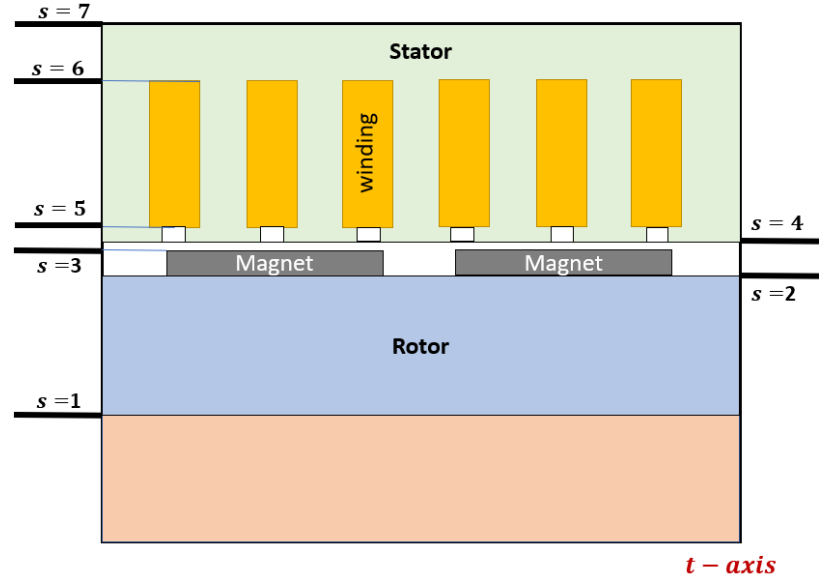
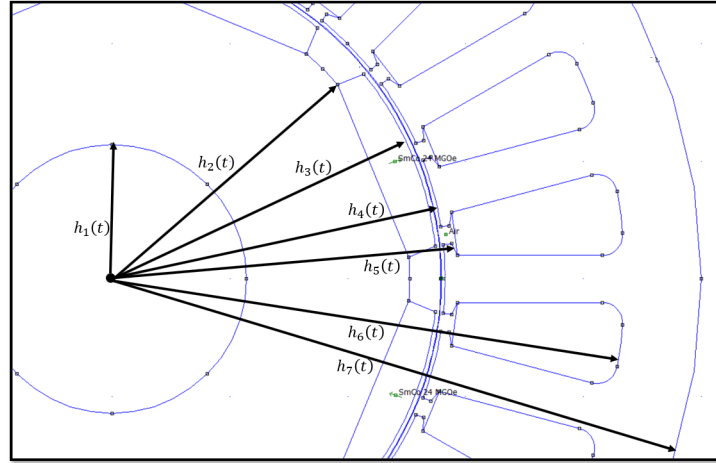


Figure 3. Fully separable domain used to compute the PGD solution taking use of the mapping detailed in Equations (9) and (10).



**Figure 4.** The integer values of the new  $s$  coordinate are placed in the positions shown in the figure.



**Figure 5.** The  $h_i(t)$  functions are used to render separable the original non-separable geometries.

## 5. PGD Parametric Solution

With the solution performance significantly improved from the fully space-separated representation  $(s, t)$ , the next natural step within the PGD rationale consists of introducing a number of model parameters as model extra-coordinates for calculating a multi-parametric solution of the vector potential.

The chosen parameters to be added to the space coordinates  $s$  and  $t$  are  $i_a, i_b, i_c$  and  $B_r$ , where  $B_r$  indicates the modulus of the remanent magnetization in the permanent magnets, with  $B_r = \mu_0 \|\mathbf{M}\|$ , while  $i_a, i_b, i_c$  are the currents of the three-phase system. In addition, for addressing the third dimension (the  $z$ -coordinate), when the 3D domain does not correspond to the 2D section extrusion, an appropriate mapping should be considered. In what follows, an extruded 3D domain, by extruding the 2D section along the  $z$ -coordinate axis, is considered.

Therefore, the goal is to obtain the parametric solution  $A_z(s, t, z, i_a, i_b, i_c, B_r)$ . When applying the PGD procedure, this function is assumed to be expressed as a finite sum of products of one-dimensional functions

$$A_z(s, t, z, i_a, i_b, i_c, B_r) = \sum_{k=1}^m X_k^1(s) X_k^2(t) X_k^3(z) X_k^4(i_a) X_k^5(i_b) X_k^6(i_c) X_k^7(B_r), \quad (12)$$

where  $m$  is the total number of sums and  $\{X_k^1, \dots, X_k^7\}$  are the sought functions for the  $k^{\text{th}}$  mode.

In addition, a PGD solution was obtained for different rotor positions, expressed by the coordinate  $\rho$ . Thus, an additional discretization is associated to the  $\rho$  coordinate. Specifically, 91 nodes are considered for discretizing the  $\pi/2$  angular interval, and, consequently, the corresponding number of solutions is performed.

Therefore, the final and most general parametric solution reads

$$A_z(s, t, z, i_a, i_b, i_c, B_r, \rho) = \begin{cases} A_z(s, t, z, i_a, i_b, i_c, B_r, \rho_1), & \rho = 0, \\ \vdots \\ A_z(s, t, z, i_a, i_b, i_c, B_r, \rho_{91}), & \rho = 90, \end{cases} \quad (13)$$

where the terms  $A_z(s, t, z, i_a, i_b, i_c, B_r, \rho_k)$  are the different computed PGD solutions. Only ninety degrees of the rotation were simulated, as the rest can be found using the symmetry of the problem.

On top of the physical space-separated solution, the electric current densities, as well as the permanent magnets, are modeled as extra coordinates of the problem. To achieve the required model, the electric current density  $J_z$ , as well as the modulus of the magnetization vector  $\mathbf{M}$ , are modeled as a function of the new space coordinates  $(s, t, z)$  as well as the corresponding additional parameters. Therefore,  $J_z$  reads

$$J_z(s, t, z, i_a, i_b, i_c, B_r, \rho_k) = \sum_{i=1}^6 \phi_i^I(s) \psi_i^I(t) \mathcal{J}_i, \quad (14)$$

where, according to Figures 6 and 7

$$\phi_i^I(s) = \begin{cases} 0, & \text{if } 1 \leq s < 5, \\ 1, & \text{if } 5 \leq s \leq 6, \\ 0, & \text{if } 6 < s \leq 7, \end{cases}$$

and

$$\psi_i^I(t) = \begin{cases} 1, & \text{for the corresponding winding position,} \\ 0, & \text{for the rest of the domain,} \end{cases}$$

with  $\mathcal{J}_i$  taking the corresponding values of  $J_z$  depending on the winding label:  $A$ ,  $-B$ ,  $C$ ,  $-A$ ,  $B$  and  $-C$ . In addition, they are arranged in the following way:  $\mathcal{J}_1$  and  $\mathcal{J}_4$  are one-dimensional functions depending on  $i_c$  (with the relation  $\mathcal{J}_1 = -\mathcal{J}_4$ ),  $\mathcal{J}_2$  and  $\mathcal{J}_5$  are one-dimensional functions depending on  $i_b$  (with the relation  $\mathcal{J}_2 = -\mathcal{J}_5$ ) and  $\mathcal{J}_3$  and  $\mathcal{J}_6$  are one-dimensional functions depending on  $i_a$  (with the relation  $\mathcal{J}_3 = -\mathcal{J}_6$ ).

Similarly,  $\mathbf{M}$  can be expressed with a finite sum involving the number of permanent magnets  $N_M$ , according to

$$\mathbf{M}(s, t, z, i_a, i_b, i_c, B_r, \rho_k) = \frac{B_r}{\mu_0} \sum_{i=1}^{N_M} \phi_i^{II}(s) \psi_i^{II}(t) \hat{\mathbf{m}}_i(s, t), \quad (15)$$

where  $\hat{\mathbf{m}}_i$  is the unit vector defining the magnetization direction of the  $i$ -magnet, according to Figure 8, and the characteristic functions defining the location of each magnet read

$$\phi_i^{II}(s) = \begin{cases} 0, & \text{if } 1 \leq s < 2, \\ 1, & \text{if } 2 \leq s \leq 3, \\ 0, & \text{if } 3 < s \leq 7, \end{cases}$$



$$\psi_i^{II}(t) = \begin{cases} 1, & \text{within the magnet location in the even numbers of magnets,} \\ -1, & \text{within the magnet location in the odd numbers of magnets.} \\ 0, & \text{for the rest of the domain.} \end{cases}$$

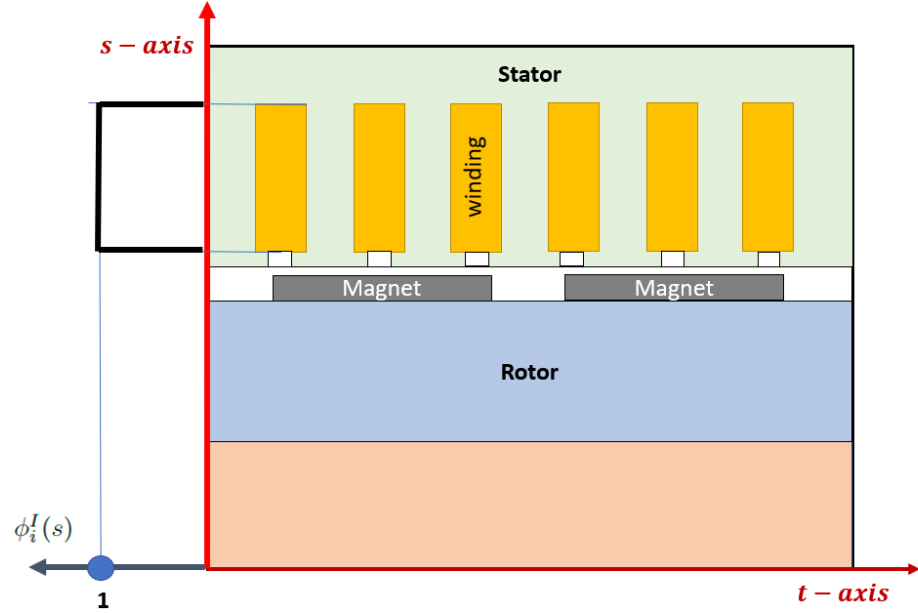


Figure 6. Illustration of  $\phi_i^I(s)$  functions involved in Equation (14).

Considering the coordinate transformation presented in Section 4 and the approximations just introduced, the problem can be formulated and solved using the standard PGD procedure. For that purpose, the reader can refer to [17–19] and the references therein.

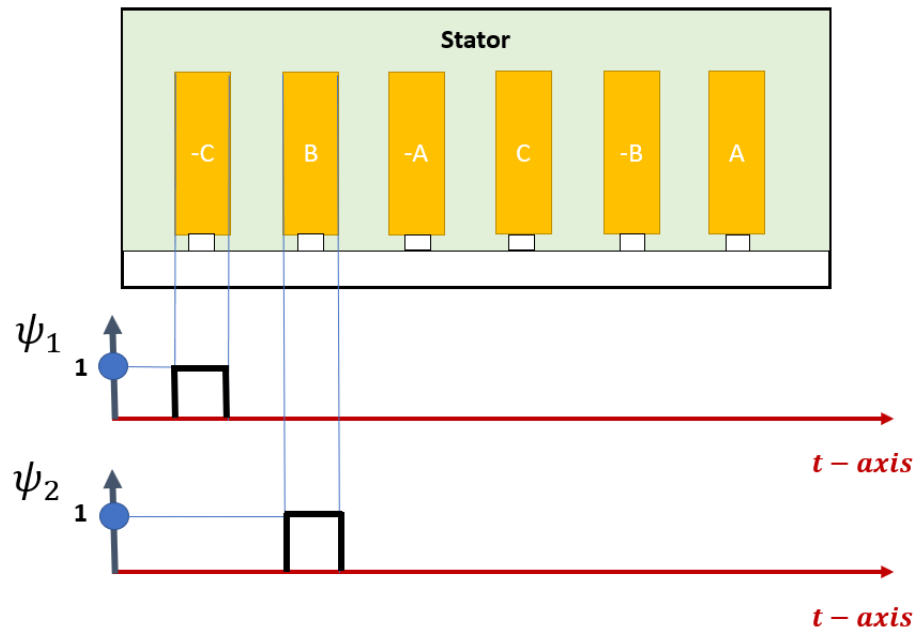


Figure 7. Illustration of functions  $\psi_1^I(t)$  and  $\psi_2^I(t)$  involved in Equation (14).

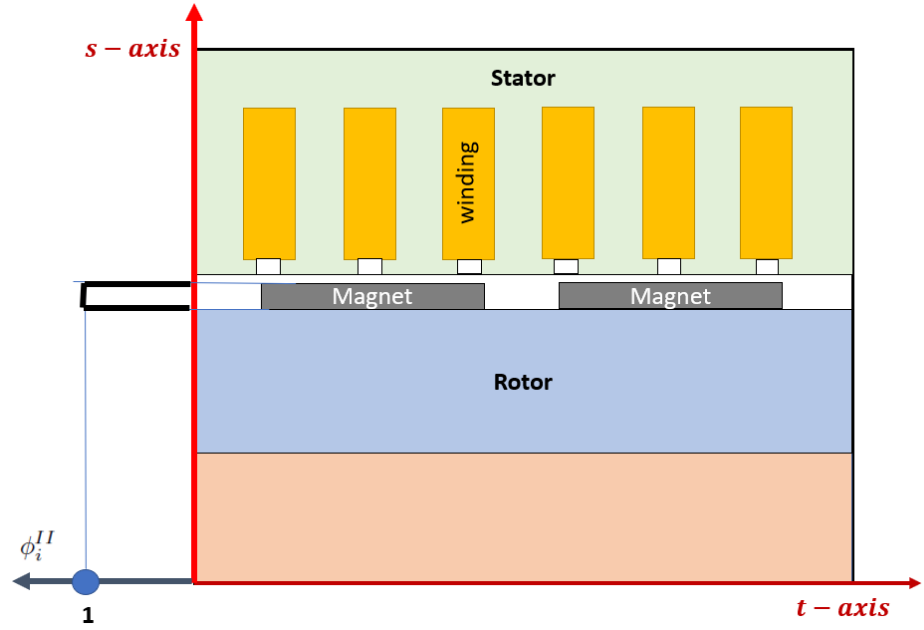


Figure 8. Functions  $\phi_i^{II}(s)$  involved in Equation (15).

## 6. Results

This section aims to analyze the motor sketched in Figure 1, whose parameters were reported in Section 3. As was indicated in the previous section (Equation (13)), a PGD parametric solution is created for each discretized rotor position  $\rho_k$  (from  $\rho_1$  to  $\rho_{91}$ ).

The results focus on one of the industrial applications where this type of solution is highly demanded: the evaluation of the electromagnetic force involved in noise and vibration analysis of electric motors. Here, the solution is specifically sought in the air-gap area to obtain the B-field in this region, and then estimate the magnetic pressure using the Maxwell stress tensor.

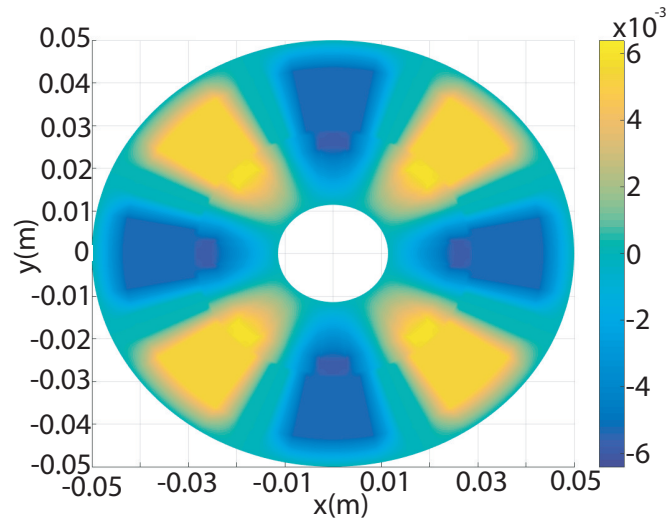
In the vibro-acoustic analysis, the following expressions are usually employed [20–22]:

$$P_n(\alpha, t) = \frac{1}{2\mu} B_n^2(\alpha, t), \quad (16)$$

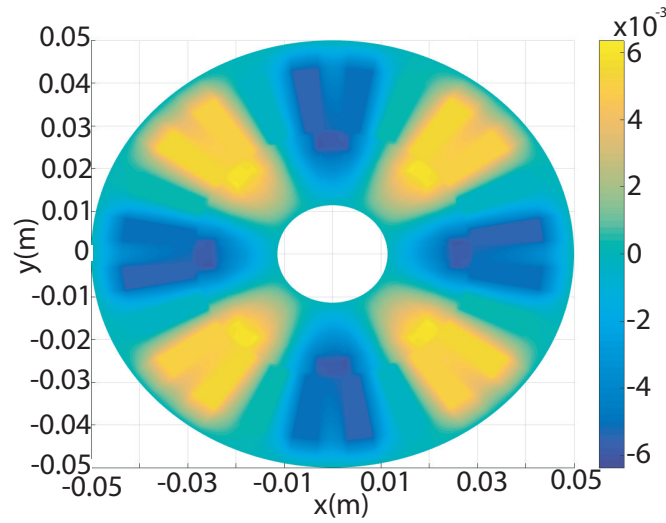
$$P_\tau(\alpha, t) \approx 0, \quad (17)$$

where  $P$  refers to the magnetic pressure,  $\alpha$  is the angle of a polar coordinate system pointing to the selected air-gap point, subscript  $n$  refers to the radial component in the air-gap midline and the subscript  $\tau$  refers to the tangential component in the air-gap midline.

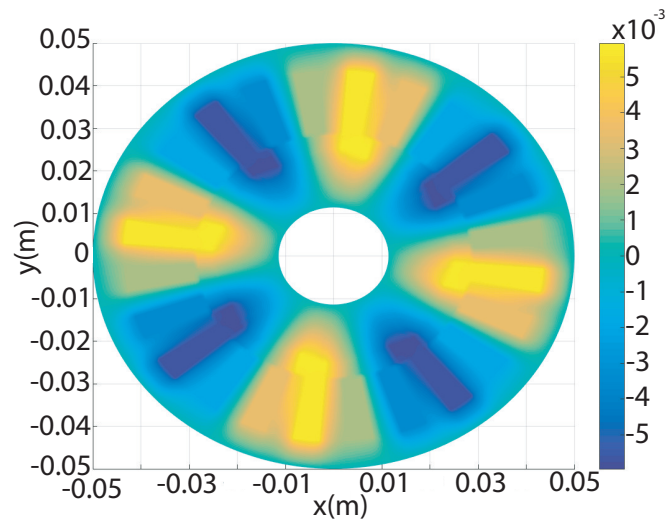
Figure 9 shows the magnetic vector potential  $A_z$  in a section of the simulated motor for different combinations of the input parameters  $i_a, i_b, i_c, B_r$  and  $\rho$ , illustrated in the physical  $(x, y)$  domain. Figure 10 illustrates the 3D results in a section of the motor assumed a simple section extrusion for a given combination of the parameters, to keep the 2D problem formulation. Even if solving the 2D magnetic problem in the 3D domain does not contribute to the solution, this remains invariant along the  $z$ -coordinate; its consideration here only aims to prove that the fully space separation can very efficiently address extremely rich 3D configurations.



(a)  $i_a = 0$  A,  $i_b = 0$  A,  $i_c = 0$  A,  $B_r = 1.01$  T and  $\rho = 0^\circ$



(b)  $i_a = -1.5$  A,  $i_b = 3$  A,  $i_c = -1.5$  A,  $B_r = 1.01$  T and  $\rho = 0^\circ$



(c)  $i_a = 0$  A,  $i_b = 0$  A,  $i_c = 0$  A,  $B_r = 1.01$  T and  $\rho = 10^\circ$

**Figure 9.**  $A_z$  for different combinations of the input parameters  $i_a$ ,  $i_b$ ,  $i_c$ ,  $B_r$  and  $\rho$ .

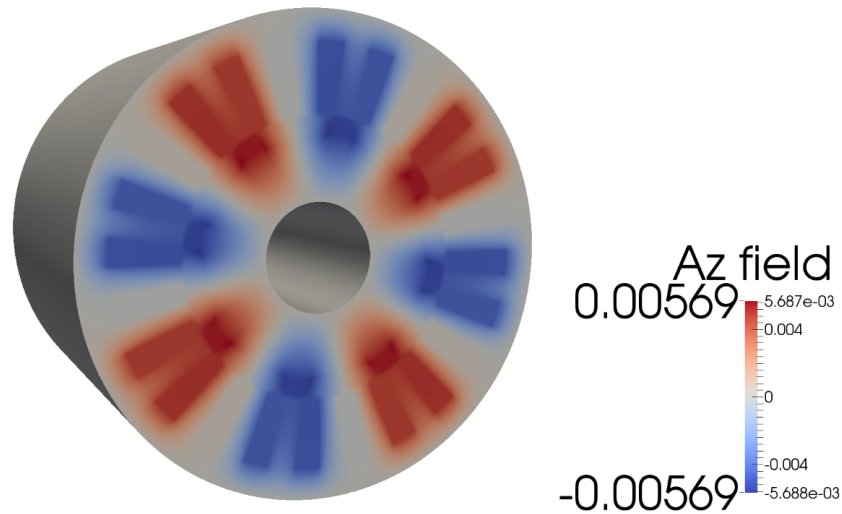


**Figure 10.**  $A_z$  in a section of the motor for  $i_a = 1.5$  A,  $i_b = 1.5$  A,  $i_c = -3$  A,  $B_r = 1.01$  T and  $\rho = 0^\circ$ .

Figures 11–13 compare the PGD solution with the one obtained by using the open-source software FEMM (assuming the FEMM solution as the reference one). An excellent agreement can be seen between the PGD-based multi-parametric solution and the reference one. However, each PGD-based parametric solution (for each rotor position,  $\rho_k$ ) is computed by using a standard laptop, in about 12 min, for a resolution equivalent to  $10^8$  different FEM simulations (the number of possible parameter choices), each of them involving an equivalent spatial resolution of 175 million nodes (degrees of freedom). Solving that number of extremely rich problems by using a standard finite element discretization becomes unreasonable. The computational efficiency increases even more when considering more parameters in the parametric solution. This constitutes the most appealing feature of PGD-based separated representations; in the present case, concerning both the 3D space (resulting in three one-dimensional approximations) and the model parameters assumed here model extra-coordinates, and are also expressed in a separated form.

As indicated previously, once the field solution is obtained, the post-processing step to obtain the magnetic pressure on the stator surface is performed, as Figures 14 and 15 reveal.

Furthermore, a comparison between the PGD and the FEMM solution is carried out on the torque, which is one of the most important quantities of interest when analyzing, for instance, the torque-speed curve. Random points of the parametric solution were checked, observing that this error was below 2% (relative error computed considering the FEMM solution as a reference).

This functionality is particularly valuable in electrical vehicles, when looking for a compromise between the torque and the normal force applied on the stator (that causes vibration and its induced noise).

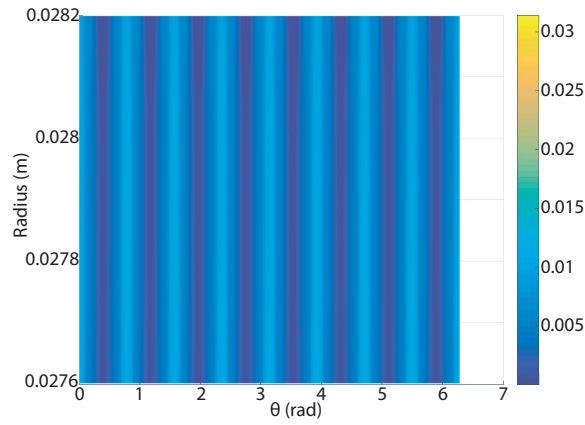


**Figure 11.** Relative error considering the PGD and the FEMM solution for the case  $(s, t) \in (\text{air gap})$ ,  $i_a = i_b = i_c = 0 \text{ A}$ ,  $B_r = 1.01 \text{ T}$ ,  $\rho = 0$  (initial position).

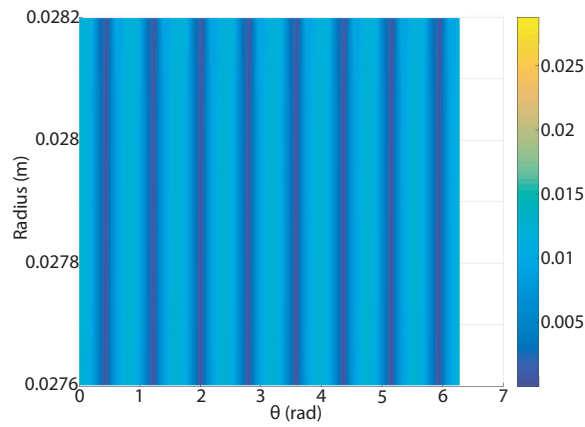


**Figure 12.** Relative error considering the PGD and the FEMM solution for the case  $(s, t) \in (\text{air gap})$ ,  $i_a = -1.5 \text{ A}$ ,  $i_b = 3 \text{ A}$ ,  $i_c = -1.5 \text{ A}$ ,  $B_r = 1.01 \text{ T}$ ,  $\rho = 0$  (initial position).

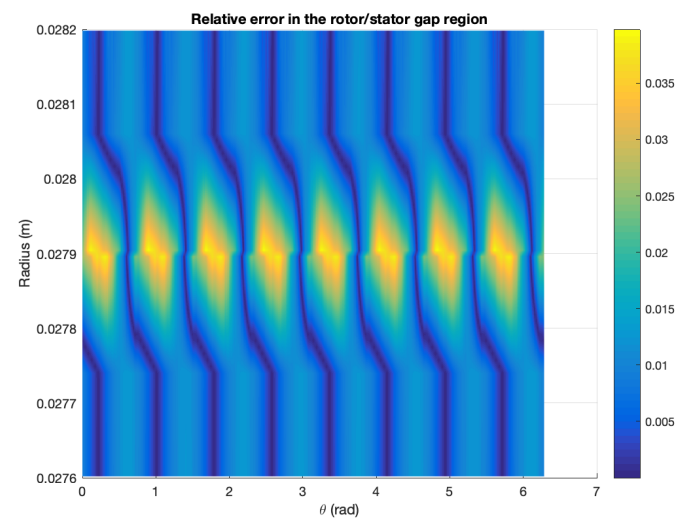


**Figure 13.** Relative error considering the PGD and the FEMM solution for the case  $(s, t) \in (\text{air gap})$ ,  $i_a = i_b = i_c = 0 \text{ A}$ ,  $B_r = 1.01 \text{ T}$ ,  $\rho = 10^\circ$ .

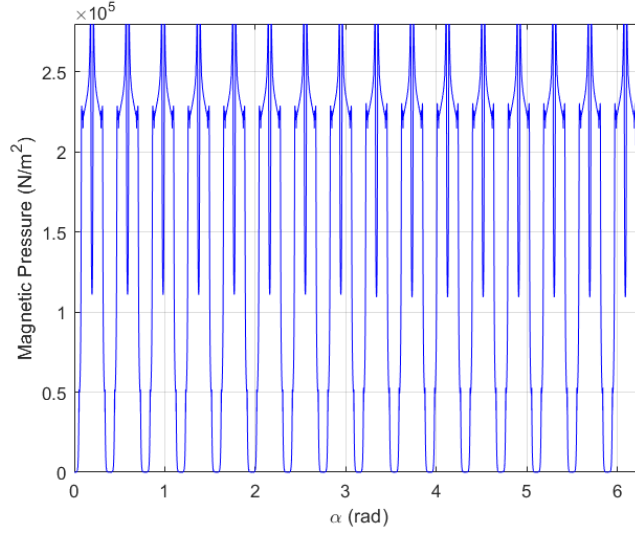


Figure 14. Magnetic pressure computed with the PGD solution for the case of Figure 11.

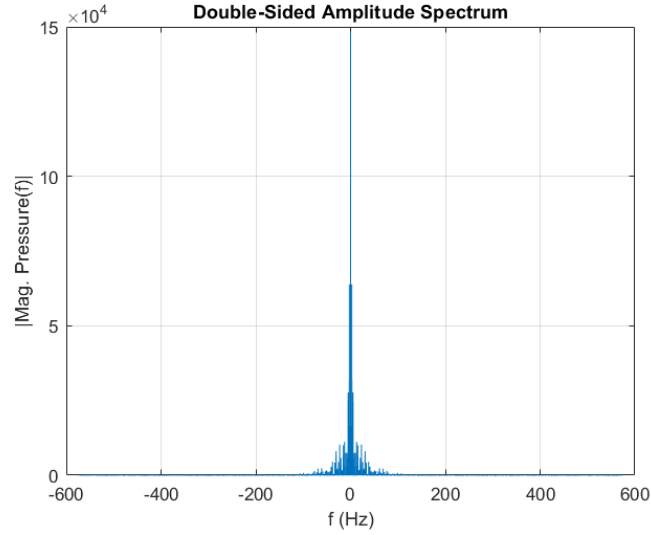


Figure 15. Fast Fourier Transform of the magnetic pressure depicted in Figure 14.

The torque directly derives from the computed solution, as described in [23], according to

$$T = \frac{D - g}{2} \frac{L}{\mu_0} \int_{l_g} B_n B_\tau dl \quad (18)$$

where  $B_n$  is the radial component of the flux density (normal to the line  $l_g$ ),  $B_\tau$  is the azimuthal component of the flux density (tangential to the air-gap midline  $l_g$ ),  $D$  is the inner stator diameter,  $L$  is the active length of the rotor in the axial direction and  $g$  is the air-gap.

Finally, it is important to note that computing a derivative of the parametric solution is easily done in the PGD framework as a pure solution post-processing, by simply taking the derivatives of the one-dimensional functions involved in the separated representation.

## 7. Conclusions

In this paper, a double separation of variables, involving both the space coordinates and the model parameters, was carried out within the PGD rationale, and was applied to the analysis of electric motors, in particular, synchronous machines. More concretely, a two-dimensional steady state analysis (magneto-static analysis) of a PMSM was studied.

In addition, an efficient coordinate transformation was proposed, which was able to proceed with a full space separation that reduced the 3D domain description from a series of one-dimensional approximations.

An excellent agreement between the FEMM software and the PGD results was noticed. The great benefit of employing the PGD is that high-dimensional parametric functions can be efficiently constructed with low computational cost.

Furthermore, the proposed approach can empower the design, optimization or inverse analysis of this type of machines because once the PGD solution is obtained in the off-line stage, it can be particularized online under the stringent real-time constraints.

**Author Contributions:** Conceptualization, F.C., J.-L.D., C.G. and A.S.; methodology, A.S. and C.G.; software, A.S. and C.G.; validation, A.S. and C.G.; resources, J.-L.D.; writing—original draft preparation, A.S.; writing—review and editing, C.G., E.C. and F.C.; supervision, F.C., J.-L.D. and N.Z.; project administration, F.C. All authors have read and agreed to the published version of the manuscript.

**Funding:** This research received no external funding.

**Institutional Review Board Statement:** Not applicable.

**Informed Consent Statement:** Not applicable.

**Data Availability Statement:** Not applicable.

**Acknowledgments:** Authors thank the Academic Editor Krzysztof Szajowski for his invitation to contribute to the present Special Volume.

**Conflicts of Interest:** The authors declare no conflict of interest.

## Appendix A. Separated Representation Constructor

The problem formulation addressed in the present paper involves the space and parameters' separate representation. For the sake of completeness, this appendix aims to illustrate, in a simple case, the construction of such a separated representation. For that purpose, we consider the 2D parametric problem

$$\nabla \cdot (\nabla u(x, y)) = k, \quad (\text{A1})$$

with uniform source term  $k$ , and homogeneous Dirichlet boundary conditions, defined in the separable domain  $\Omega = \Omega_x \times \Omega_y$ . We wish to compute *at once* a general solution of the problem for *all* values of  $k$  in a given interval of values  $\Omega_k$ .

In the PGD framework, we thus consider the source term  $k$  as an extra-coordinate, in addition to the space coordinates  $x$  and  $y$ . The problem (A1) is now defined for  $(x, y, k) \in \Omega_x \times \Omega_y \times \Omega_k$ .

Thus, instead of solving a series of diffusion problems for different discrete values of the source term, we wish to solve a more general problem. The price to pay is, of course, an increase in the problem dimensionality. This is not a major issue for the PGD, whose computational complexity is scaled only linearly (and not exponentially) with the space dimension. Moreover, as the domain  $\Omega$  is separable, a fully separated representation can be envisaged, which reduces the parametric 2D problem to a sequence of three one-dimensional problems: the first involving the  $x$ -coordinate, the second the  $y$ -coordinate and the third and last, the  $k$ -extra-coordinate, as described in what follows.

The extended weighted residual form of (A1) reads

$$\int_{\Omega_x \times \Omega_y \times \Omega_k} u^* \left( \frac{\partial^2 u}{\partial x^2} + \frac{\partial^2 u}{\partial y^2} - k \right) dx dy dk = 0, \quad (\text{A2})$$

for all suitable test functions  $u^*$ .

The separated form of the searched solution reads

$$u(x, y, k) = \sum_{i=1}^N X_i(x) Y_i(y) K_i(k), \quad (\text{A3})$$

where each term will be computed one at a time, enriching the PGD solution until reaching the convergence.

At step  $n$  of the PGD algorithm, the following approximation is assumed to already be calculated

$$u^{n-1}(x, y, k) = \sum_{i=1}^{n-1} X_i(x) Y_i(y) K_i(k), \quad (\text{A4})$$

and aims to compute the functions involved in the  $n$ -mode,  $X_n(x)$ ,  $Y_n(y)$  and  $K_n(k)$ , according to

$$u^n = u^{n-1} + X_n(x) Y_n(y) K_n(k). \quad (\text{A5})$$

The weighted residual form (A2) defines a non-linear problem, which is solved iteratively. Each iteration  $r$  of the nonlinear solver consists of the three steps

1. Compute  $X_n^r(x)$  from the other two functions taken at the previous nonlinear iteration, i.e.,  $Y_n^{r-1}(y)$  and  $K_n^{r-1}(k)$ ;
2. Compute  $Y_n^r(y)$  from  $X_n^r(x)$  and  $K_n^{r-1}(k)$ ;
3. Compute  $K_n^r(k)$  from  $X_n^r(x)$  and  $Y_n^r(y)$ .

In what follows, these three calculations are detailed.

- Computing  $X_n^r(x)$  from  $Y_n^{r-1}(y)$  and  $K_n^{r-1}(k)$  with the trial and test functions given by

$$u^{n,r}(x, y, k) = \sum_{i=1}^{n-1} X_i(x) Y_i(y) K_i(k) + X_n^r(x) Y_n^{r-1}(y) K_n^{r-1}(k), \quad (\text{A6})$$

and

$$u^*(x, y, k) = X^*(x) Y_n^{r-1}(y) K_n^{r-1}(k), \quad (\text{A7})$$

respectively, the weighted residual formulation reads

$$\begin{aligned} & \int_{\Omega_x \times \Omega_y \times \Omega_k} X^*(x) Y_n^{r-1}(y) K_n^{r-1}(k) \\ & \left( \frac{d^2 X_n^r(x)}{dx^2} Y_n^{r-1}(y) K_n^{r-1}(k) + X_n^r(x) \frac{d^2 Y_n^{r-1}(y)}{dy^2} K_n^{r-1}(k) \right) dx dy dk = \\ & \int_{\Omega_x \times \Omega_y \times \Omega_k} X^*(x) Y_n^{r-1}(y) K_n^{r-1}(k) \mathcal{R}^{n-1} dx dy dk, \end{aligned} \quad (\text{A8})$$

where  $\mathcal{R}^{n-1}$  is the residual related to  $u^{n-1}(x, y, k)$ ,

$$\mathcal{R}^{n-1} = k - \sum_{i=1}^{n-1} \left( \frac{d^2 X_i(x)}{dx^2} Y_i(y) K_i(k) + X_i(x) \frac{d^2 Y_i(y)}{dy^2} K_i(k) \right). \quad (\text{A9})$$

Since all functions of the  $y$ -coordinate and the source term  $k$ -extra-coordinate are known, we can integrate (A8) over  $\Omega_y \times \Omega_k$ , to obtain

$$\int_{\Omega_x} X^*(x) \left( \alpha^{x,r} \frac{d^2 X_n^r(x)}{dx^2} + \beta^{x,r} X_n^r(x) - \gamma^{x,r} + \right.$$



$$+ \sum_{i=1}^{n-1} \left( \delta_i^{x,r} \frac{d^2 X_i(x)}{dx^2} + \zeta_i^{x,r} X_i(x) \right) dx = 0, \quad (\text{A10})$$

where coefficients  $\alpha^{x,r}$ ,  $\beta^{x,r}$ ,  $\gamma^{x,r}$ ,  $\delta_i^{x,r}$  and  $\zeta_i^{x,r}$  result from the integrals in  $\Omega_y \times \Omega_k$  of the different products of functions  $Y_i(y)$ ,  $K_i(k)$ ,  $Y_n^{r-1}(y)$  and  $K_n^{r-1}$  involved in Equation (A8).

With Equation (A10) valid for any function  $X^*(x)$ , we can extract its associated strong form

$$\alpha^{x,r} \frac{d^2 X_n^r(x)}{dx^2} + \beta^{x,r} X_n^r(x) = \gamma^{x,r} - \sum_{i=1}^{n-1} \left( \delta_i^{x,r} \frac{d^2 X_i(x)}{dx^2} + \zeta_i^{x,r} X_i(x) \right), \quad (\text{A11})$$

whose solution results in the searched function  $X_n^r(x)$ .

- Computing  $Y_n^r(y)$  from  $X_n^r(x)$  and  $K_n^{r-1}(k)$   
With the test function given by

$$u^*(x, y, k) = X_n^r(x) Y^*(y) K_n^{r-1}(k), \quad (\text{A12})$$

and following the same rationale as previously, after integrating the weighted residual form in  $\Omega_x \times \Omega_k$  and extracting the resulting strong form, we obtain

$$\alpha^{y,r} \frac{d^2 Y_n^r(y)}{dy^2} + \beta^{y,r} Y_n^r(y) = \gamma^{y,r} - \sum_{i=1}^{n-1} \left( \delta_i^{y,r} \frac{d^2 Y_i(y)}{dy^2} + \zeta_i^{y,r} Y_i(y) \right). \quad (\text{A13})$$

- Computing  $K_n^r(k)$  from  $X_n^r(x)$  and  $Y_n^r(y)$   
Finally, with the test function given by

$$u^*(x, y, k) = X_n^r(x) Y_n^r(y) K^*(k), \quad (\text{A14})$$

and following the same rationale as previously, after integrating the weighted residual form in  $\Omega_x \times \Omega_y$  and extracting the resulting strong form, we obtain

$$\beta^{k,r} K_n^r(k) = \gamma^{k,r} k - \sum_{i=1}^{n-1} \zeta_i^{k,r} K_i(k). \quad (\text{A15})$$

## References

1. Farzamfar, M.; Belahcen, A.; Rasilo, P.; Clenet, S.; Pierquin, A. Model order reduction of electrical machines with multiple inputs. *IEEE Trans. Ind. Appl.* **2017**, *53*, 3355–3360. [[CrossRef](#)]
2. Kumar, M.S.; Harish, S.; Apparao, A.D. Design of PID controller via novel model order reduction technique. *Int. J. Adv. Res. Comput. Commun. Eng.* **2015**, *4*, 278–281.
3. Chinesta, F.; Keunings, R.; Leygue, A. *The Proper Generalized Decomposition for Advanced Numerical Simulations: A Primer*; Springer Briefs: Berlin, Germany, 2013.
4. Cueto, E.; Gonzalez, D.; Alfaro, I. *Proper Generalized Decompositions: An Introduction to Computer Implementation with Matlab*, 1st ed.; Springer Briefs: Berlin, Germany, 2016.
5. Bucolo, M.; Buscarino, A.; Famoso, C.; Fortuna, L.; Frasca, M. Control of imperfect dynamical systems. *Nonlinear Dyn.* **2019**, *98*, 2989–2999. [[CrossRef](#)]
6. Sancarlos-González, A.; Pineda Sanchez, M.; Puche-Panadero, R.; Sapena-Bañó, A.; Riera-Guasp, M.; Martinez-Roman, J.; Perez-Cruz, J.; Roger-Folch, J. Application of the parametric proper generalized decomposition to the frequency-dependent calculation of the impedance of an AC line with rectangular conductors. *Open Phys.* **2017**, *15*. [[CrossRef](#)]
7. Henneron, T.; Clenet, S. Application of the Proper Generalized Decomposition to Solve MagnetoElectric Problem. *IEEE Trans. Magn.* **2017**, *54*, 1–4. [[CrossRef](#)]
8. Sancarlos, A.; Cameron, M.; Abel, A.; Cueto, E.; Duval, J.; Chinesta, F. From ROM of electrochemistry to AI-based battery digital and hybrid twin. *Arch. Comput. Methods Eng.* **2020**, 1–37. [[CrossRef](#)]
9. Ghnatio, C.; Cueto, E.; Falco, A.; Duval, J.L.; Chinesta, F. Spurious-free interpolations for non-intrusive PGD-based parametric solutions: Application to composites forming processes. *Int. J. Mater. Form.* **2021**, *14*, 83–95. [[CrossRef](#)]

10. Ghnatios, C.; Abisset, E.; Ammar, A.; Cueto, E.; Duval, J.L.; Chinesta, F. Advanced separated spatial representations for hardly separable domains. *Comput. Methods Appl. Mech. Eng.* **2019**, *354*, 802–819. [[CrossRef](#)]
11. Chinesta, F.; Leygue, A.; Bordeu, F.; Aguado, J.; Cueto, E.; Gonzalez, D.; Alfaro, I.; Ammar, A.; Huerta, A. Parametric PGD based computational vademecum for efficient design, optimization and control. *Arch. Comput. Methods Eng.* **2013**, *20*, 31–59. [[CrossRef](#)]
12. Chinesta, F.; Huerta, A.; Rozza, G.; Willcox, K. Model Order Reduction. In *The Encyclopedia of Computational Mechanics*, 2nd ed.; Stein, E., de Borst, R., Hughes, T., Eds.; John Wiley & Sons, Ltd.: Hoboken, NJ, USA, 2015.
13. Salon, S.J. *Finite Element Analysis of Electrical Machines*; Springer Science + Business Media: New York, NY, USA, 1995.
14. Meeker, D.C. Finite Element Method Magnetics. *FEMM* **2010**, *4*, 32.
15. Ghnatios, C.; Xu, G.; Visonneau, M.; Leygue, A.; Chinesta, F.; Cimetiere, A. On the space separated representation when addressing the solution of PDE in complex domains. *Discret. Contin. Dyn. Syst.* **2016**, *9*, 475–500.
16. Ghnatios, C.; Montes, N.; Tertrais, H.; Duval, J.; Abisset-Chavanne, E.; Falco, A.; Chinesta, F. Towards parametric RTM processes: The interpolative mapping. *Proc. Am. Inst. Phys. Proc.* **2019**, *2113*, 100004. [[CrossRef](#)]
17. Ghnatios, C. Simulation Avancée des Problèmes Thermiques Rencontrés Lors de la Mise en Forme des Composites. Ph.D. Thesis, Ecole Centrale Nantes, Nantes, France, 2012.
18. Ghnatios, C.; Mathis, C.H.; Simic, R.; Spencer, N.D.; Chinesta, F. Modeling soft, permeable matter with the proper generalized decomposition (PGD) approach, and verification by means of nanoindentation. *Soft Matter* **2017**, *13*, 4482–4493. [[CrossRef](#)] [[PubMed](#)]
19. Cueto, E.; Ghnatios, C.; Chinesta, F.; Montes, N.; Sanchez, F.; Falco, A. Improving computational efficiency in LCM by using computational geometry and model reduction techniques. *Key Eng. Mater.* **2014**, *611–612*, 339–343. [[CrossRef](#)]
20. Pile, R.; Devillers, E.; Le Besnerais, J. Comparison of Main Magnetic Force Computation Methods for Noise and Vibration Assessment in Electrical Machines. *IEEE Trans. Magn.* **2018**, *54*, 1–13. [[CrossRef](#)]
21. Xu, X.; Han, Q.; Chu, F. Review of Electromagnetic Vibration in Electrical Machines. *Energies* **2018**, *11*, 1779. [[CrossRef](#)]
22. Haas, S.; Ellermann, K. Development and Analysis of Radial Force Waves in Electrical Rotating Machines. *Tech. Mech.* **2017**, *37*, 218–225. [[CrossRef](#)]
23. Bianchi, N. *Electrical Machine Analysis Using Finite Elements*; CRC Press Taylor & Francis Group: Boca Raton, FL, USA, 2005. [[CrossRef](#)]